Bone 161 (2022) 116432

Contents lists available at ScienceDirect

Bone

journal homepage: www.elsevier.com/locate/bone

Full Length Article

In vivo microCT-based time-lapse morphometry reveals anatomical site-specific differences in bone (re)modeling serving as baseline parameters to detect early pathological events

Sarah A.E. Young [a], Maximilian Rummler [a,b,c], Hubert M. Taïeb [a], Daniela S. Garske [a], Agnes Ellinghaus [d], Georg N. Duda [d], Bettina M. Willie [b,c], Amaia Cipitria [a,e,f,*]

[a] Department of Biomaterials, Max Planck Institute of Colloids and Interfaces, Potsdam, Germany
[b] Research Centre, Shriners Hospital for Children-Canada, Montreal, Canada
[c] Department of Pediatric Surgery, McGill University, Montreal, Canada
[d] Julius Wolff Institute & Berlin Institute of Health Center for Regenerative Therapies, Berlin Institute of Health and Charité-Universitätsmedizin Berlin, Berlin, Germany
[e] Biodonostia Health Research Institute, Group of Bioengineering in Regeneration and Cancer, San Sebastian, Spain
[f] IKERBASQUE, Basque Foundation for Science, Bilbao, Spain

ARTICLE INFO

Keywords:
In vivo microcomputed tomography (microCT)
Time-lapse morphometry
Bone (re)modeling baseline parameters
Tibia *vs.* femur
Early osteolytic events

ABSTRACT

The bone structure is very dynamic and continuously adapts its geometry to external stimuli by modeling and remodeling the mineralized tissue. *In vivo* microCT-based time-lapse morphometry is a powerful tool to study the temporal and spatial dynamics of bone (re)modeling. Here an advancement in the methodology to detect and quantify site-specific differences in bone (re)modeling of 12-week-old BALB/c nude mice is presented. We describe our method of quantifying new bone surface interface readouts and how these are influenced by bone curvature. This method is then used to compare bone surface (re)modeling in mice across different anatomical regions to demonstrate variations in the rate of change and spatial gradients thereof. Significant differences in bone (re)modeling baseline parameters between the metaphyseal and epiphyseal, as well as cortical and trabecular bone of the distal femur and proximal tibia are shown. These results are validated using conventional static *in vivo* microCT analysis. Finally, the insights from these new baseline values of physiological bone (re) modeling were used to evaluate pathological bone (re)modeling in a pilot breast cancer bone metastasis model. The method shows the potential to be suitable to detect early pathological events and track their spatio-temporal development in both cortical and trabecular bone. This advancement in (re)modeling surface analysis and defined baseline parameters according to distinct anatomical regions will be valuable to others investigating various disease models with site-distinct local alterations in bone (re)modeling.

1. Introduction

The skeleton serves multiple functions: mechanical functions for structural support, locomotion or protection of organs, endocrine function serving as mineral reservoir, and maintenance of hematopoietic cells. For this reason, the organ bone is highly dynamic and is continuously adapting to external stimuli and changing with damage repair. Bone mechanical properties are connected at two length scales: the whole-bone properties and the tissue-level properties. The description of the tissue-level entails the use of bone morphological parameters to describe differences and changes in the bone structure [1]. One major focus has been describing dynamic changes in the bone structure, referred to as bone (re)modeling [2–4]. Bone modeling on one hand, describes the removal or addition of bone material with the aim of structural adaptation, but without a spatio-temporal connection between new mineralization and erosion [5]. In contrast, bone remodeling serves the purpose of bone maintenance and damage repair, whereby osteoclasts are recruited to a specific site leading to bone erosion, which is then followed by the recruitment of osteoblasts and consequently new mineralization. Bone surface (re)modeling in rodents constitutes an important area of research, since a broad variety of diseases and functions are studied with this model organism and thus well-established baselines of bone (re)modeling parameters for healthy animals are required.

* Corresponding author at: Max Planck Institute of Colloids and Interfaces, Am Mühlenberg 1, 14476 Potsdam, Germany.
E-mail address: amaia.cipitria@mpikg.mpg.de (A. Cipitria).

https://doi.org/10.1016/j.bone.2022.116432
Received 3 February 2022; Received in revised form 9 May 2022; Accepted 9 May 2022
Available online 12 May 2022

The standard method to study bone (re)modeling in mice is two-dimensional (2D) dynamic histomorphometry using fluorochrome labeling [3,4,6–9]. In dynamic histomorphometry, fluorescent dyes are injected into the living animal and integrated in newly forming bone while this is being mineralized. As a result, the mineralization front is labeled at the injection time point. By using several different dyes at specific time points, the evolution of mineralization as well as the bone turnover can be studied. However, to obtain the (re)modeling information the animal has to be sacrificed, leaving no room for *in vivo* monitoring. An alternative method to quantify bulk changes in bone *in vivo* and in 3D is static microcomputed tomography (microCT). *Ex vivo* microCT has significantly advanced the possibilities to quantify the microstructure and density of the bone at a given time point [10–15]. *In vivo* microCT allows longitudinal assessment of changes in the microstructure and density [16]. However, the dynamic evolution of the (re) modeled bone over time, as well as the spatial localization of specific formation and resorption events, is not obtained.

To acquire this spatio-temporal information of how bone is (re) modeled, dynamic *in vivo* microCT-based time-lapse morphometry has been developed by several research groups over the last years. The method allows one to temporally and spatially monitor both bone mineralization and erosion events [17–21]. With this method, microCT scans of the same animal are acquired *in vivo* at different time points, repositioning the animal as similarly as possible at each scan. Next, the datasets at later time points are geometrically aligned (registered) with respect to an earlier time point to evaluate where bone has been eroded or newly mineralized. The method allows quantification of volumes, surfaces, thickness/depth and rates of bone mineralization and erosion. The accuracy of the time-lapse method used and further developed in the current study, was previously validated by comparing with 2D dynamic histomorphometry using fluorochrome labeling in both cortical [18] and trabecular bone [22]. Birkhold *et al.* showed differences in bone (re)modeling between the endosteal and periosteal surface [23] as well as between regions of the cortical bone (proximal metaphysis and mid-diaphysis) from the same limb [24]. In addition, the precision of the method was previously reported [18,25]. Schulte *et al.* [19] and Birkhold *et al.* [18] quantitatively described the mineralized and eroded surface by looking at the interface between constant and newly formed bone, which is the original bone surface at the reference day; while the eroded surface was defined as the interface between eroded bone and soft tissue, which is the bone surface at the later time point. Thus, the readout parameters for newly mineralized and eroded surface area can be expanded because only one of two potential interfaces for each region is described and these surfaces are highly influenced by curvature. In this work, we describe the advancement of this method.

Here, we aim to use dynamic *in vivo* microCT-based time-lapse morphometry to examine bone (re)modeling in anatomical site-specific regions of healthy, skeletally mature mice, thus obtaining baseline parameters for physiological bone (re)modeling. To do so, we compare (re) modeling between the metaphyseal and epiphyseal, cortical and trabecular sites at the distal femur and proximal tibia. We hypothesize that these generated baseline parameters can be used to detect pathological bone (re)modeling and track its spatio-temporal development. This could open up the opportunity to use time-lapse morphometry to characterize the onset and progression of disease models with altered bone (re)modeling, including cancer-related osteolytic and osteoblastic pathologies.

2. Materials and methods

2.1. Animal model

Female 12-week-old BALB/c nude mice (CAnN.Cg-*Foxn1*^{nu}/Crl, Charles River, Sulzfeld, Germany) were received and acclimatized in the animal facility of the Charité - Universitätsmedizin Berlin (n = 7). The mice were housed 2–4 animals per cage with *ad libitum* access to food and water. Mice (n = 7) were injected at day 4 (after reference scan at day 0, Fig. 1A) into the left ventricle of the heart (one injection per mouse), using a 27 G needle, under ultrasound guidance (Vevo2100, FUJIFILM VisualSonics Inc., Canada). The mice used to study physiological bone (re)modeling (n = 6) were injected with PBS to ensure comparability after such intervention, while the one mouse used in the pilot tumor model study (n = 1) was injected with MDA-MB-231-1833 BoM cells (5×10^5 cells in 100 μL). The animals received Carprofen (CP-Pharma Handelsgesellschaft mbH, Burgdorf, Germany) and Buprenorphine (CP-Pharma Handelsgesellschaft mbH, Burgdorf, Germany) as analgesic drugs during and after the injection. During longitudinal *in vivo* imaging, the animals were anesthetized using isoflurane (CP-Pharma Handelsgesellschaft mbH, Burgdorf, Germany) at 1–2% with oxygen as a carrier and the eyes were protected from drying with Pan-Ophtal gel (Dr. Winzer Pharma GmbH, Berlin, Germany). The initial average animal weight was 20.5 ± 2 g. The weight at sacrifice for the mice used to study physiological bone (re)modeling 45 days later was 20.2 ± 1 g. All animal experiments were carried out according to the policies and procedures approved by local legal research animal welfare representatives (LAGeSo Berlin, G0224/18).

2.2. Cell culture

MDA-MB-231-1883 BoM cells were provided by Dr. Joan Massagué and purchased from the Antibody and Bioresource Core Facility of the Memorial Sloan Kettering Cancer Center, USA. Briefly, the subclone 1833 is a bone tropic human cell line derived from a metastasis formed by MDA-MB-231 TGL cells hosted in a mouse [26,27], which in turn are MDA-MB-231 (ATCC ® HTB-26™) human epithelial breast cancer cells stably transduced with a lentivirus expressing a triple-fusion reporter [28].

MDA-MB-231-1883 BoM cells were cultured in low glucose Dulbecco's Modified Eagle's Medium (Sigma-Aldrich, Taufkirchen, Germany) supplemented with 1% penicillin/streptomycin (Gibco) and 10% fetal bovine serum (FBS superior, Sigma-Aldrich, Taufkirchen, Germany). The cells were grown at 37 °C with 5% CO_2 and regular passaging.

2.3. Longitudinal in vivo microCT image acquisition

2.3.1. Physiological bone (re)modeling

Longitudinal imaging of the hind limbs of the six mice used to study physiological bone (re)modeling was performed with a high resolution microCT (U-CT^{HR}, MILabs, Netherlands). The X-ray tube was operated at 50 kVp source voltage and 210 μA source current. Images were acquired at a step angle of 0.375° with 2 projections per step (75 ms exposure time), over a range of 360° and with a resolution of 8.5 μm voxel size. Two aluminum filters with 100 μm and 400 μm thickness were used. To prevent motion artifacts, the anesthetized mice were positioned using an animal bed with the hind limbs restrained (Fig. S1A). The scan region was determined on an X-ray scout view and included the entire femur and tibia of both hind limbs as shown in Fig. S1B. The scans were reconstructed using the MILabs Reconstruction software and a projection filter (Hann) was applied in the process. The scanner was calibrated before every scan using the internal calibration system.

The animals were scanned with the microCT for a reference scan (day 0, 12-week-old). After 17 days, the animals were scanned weekly up until 45 days (on day 17, 24, 31, 38 and 45) as shown in Fig. 1A. The anesthetized mice were sacrificed by cervical dislocation. The hind limbs were harvested and fixed with 4% paraformaldehyde (PFA) in phosphate-buffered saline (PBS) for 12 h at 4 °C and stored in PBS until further processing.

2.3.2. Pathological bone (re)modeling

The hind limbs of the pilot tumor mouse (n = 1) were imaged *in vivo* with microCT (vivaCT 40, Scanco Medical, Switzerland). The scans of

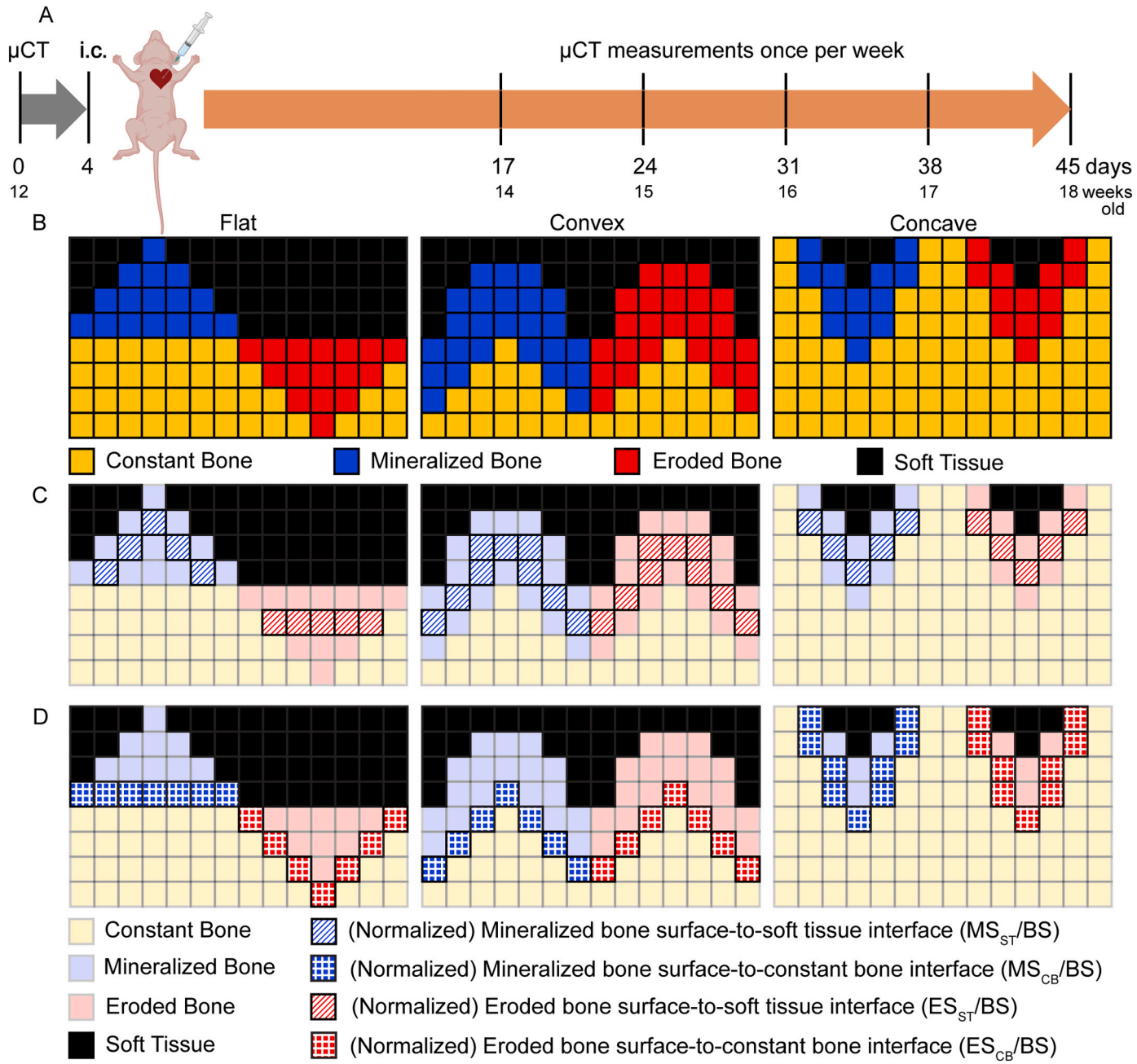

Fig. 1. Experimental design and sketch of how four distinct interfaces are strongly influenced by surface curvature. (A) Timeline of the experimental set-up with the reference microCT scan at day 0, injection at day 4 and weekly microCT measurements once per week after day 17 (created with BioRender.com). (B) Schematic of the output of a microCT scan registration, with mineralized bone (blue) and eroded bone (red), constant bone (yellow) and soft tissue (black), on a flat, convex or concave surface. Different definitions of forming and resorbing bone surfaces on the interface with (C) soft tissue or with (D) constant bone, giving rise to two distinct normalized mineralized bone surfaces (MS$_{ST}$/BS and MS$_{CB}$/BS) and two distinct normalized eroded bone surfaces (ES$_{ST}$/BS and ES$_{CB}$/BS). The schematic shows constant bone (light yellow), mineralized bone (light blue), eroded bone (light red) and soft tissue (black), as well as MS$_{ST}$/BS (lined blue), MS$_{CB}$/BS (hatched blue), ES$_{ST}$/BS (lined red) and ES$_{CB}$/BS (hatched red). (For interpretation of the references to colour in this figure legend, the reader is referred to the web version of this article.)

the hind limbs were performed at 55 kVp source voltage and 145 μA source current, 600 ms exposure time, no frame averaging, over a range of 180° and with a resolution of 10.5 μm voxel size. The animal was scanned on a custom-made bed to avoid motion artifacts.

The animal was scanned with the microCT for a reference scan (day 0, 12-week-old). Additional scans were performed at day 10, 17, 24 and 28 (*post mortem*). After sacrifice the hind limbs were harvested and fixed with 4% PFA in PBS for 12 h at 4 °C and stored in PBS until further processing.

2.4. Dynamic microCT-based time-lapse bone morphometry

The analysis was performed in accordance with Birkhold *et al.* [18,22]. To assess morphological changes due to physiological bone (re) modeling, microCT scans of each time point (day 17, 24, 31, 38 and 45) were compared to the reference scan at day 0, which ensures full information for all time points and no loss of events by changing the reference scan. We analyzed the right limb of each of the six mice and one pilot tumor mouse. The regions of interest (ROIs) were set at the distal femoral metaphysis and the proximal tibial metaphysis. Each ROI

started at the end of the non-mineralized growth plate, on the interface where the primary spongiosa of the metaphysis is found, and extended towards the diaphysis for 10% of the total bone length. The ROI included both primary and secondary spongiosa of the metaphysis. The entire epiphysis and other connected bones were manually segmented from the metaphysis. The threshold was determined using the 3D Otsu-Method to distinguish mineralized tissue from water and soft tissue [29] (tool provided by the software Amira 2020.1, Thermo Fisher Scientific, MA, USA). The thresholds are reported in the supplementary information, Table S1 for the tibiae and in Table S2 for the femora.

The registration process and following evaluation was performed in accordance with Birkhold *et al.* [18,22]. The images were pre-processed and aligned using Amira. During the pre-processing step, the dataset was pre-cropped to the respective ROI and the epiphysis, as well as other connected bones such as the fibula, were manually removed.

For the registration process, later time point images were registered onto the reference image (day 0) using a 3D rigid registration algorithm [18]. The threshold determined as described above was used to exclude background noise for the registration, while keeping the grey scale of the respective bone region. A hierarchical strategy was chosen for the registration to avoid local minima, starting with coarse resampling and proceeding to finer resolutions under visual control to ensure correct registration. After the registration, the images were transformed into the same coordinate system using a Lanczos interpolation, keeping the voxel size the same. The images were then cropped according to the corresponding ROI.

Then the ROIs were segmented into trabecular and cortical bone and evaluated using custom-made MATLAB (MATLAB 2018a; The Mathworks, Inc. Natick, MA, USA) scripts. Bone morphological changes were evaluated as previously described [18]: normalized newly mineralized bone volume (MV/BV) (normalized parameters are divided by the respective bone volume or bone surface of the reference scan), normalized mineralized bone surface-to-constant bone interface (MS_{CB}/BS), 3D mineral apposition rate (MAR, mean thickness of formed bone in μm/day), normalized eroded bone volume (EV/BV), normalized eroded bone surface-to-soft tissue interface (ES_{ST}/BS), as well as 3D mineral resorption rate (MRR, mean depth of resorbed bone in μm/days). In addition, two new surface parameters were included: the normalized mineralized bone surface-to-soft tissue interface (MS_{ST}/BS) and the normalized eroded bone surface-to-constant bone interface (ES_{CB}/BS). All surfaces are depicted in Fig. 1C and D. These two additional interfaces complement the already existing parameters and were evaluated in an analogue manner. Briefly, for each case only the concerning voxels, being constant bone, mineralized or eroded bone voxels, were taken into consideration. The first layer of voxels was disregarded due to partial volume effects, leaving the second most outward layer of voxels to be considered as the soft tissue interface, while the constant bone interface was evaluated by expanding the constant bone surface by one voxel. For the surface evaluation only one layer of voxels was taken into account. The different interfaces were calculated independently of each other and can thus in specific cases contain the same voxels, as depicted in Fig. 1C and D. The description of the surfaces is not influencing the analysis of volumetric parameters, which are calculated from all bone voxels independently. All parameters are calculated in the same way for cortical and trabecular bone. A full list of all analyzed parameters, their abbreviation, definition and unit is summarized in Table 1 below.

2.5. Static microCT-based bone morphometry

Static *in vivo* microCT-based bone analysis was performed on the same pre-processed images for each time point (day 0, 17, 24, 31, 38 and 45), using the same 3D Otsu determined threshold as was used for the dynamic time-lapse analysis. The separation of cortical and trabecular bone was achieved with the help of morphological operations in MATLAB, similar to the dynamic time-lapse analysis, as described by Birkhold *et al.* [18]. The bone parameters investigated were: total volume (TV), bone volume (BV) and bone volume fraction (BV/TV) for both cortical and trabecular bone, as well as bone surface over bone volume (BS/BV) for cortical bone. The parameters were calculated in MATLAB following the standard procedures as described by Bouxsein *et al.* [10]. Briefly, for cortical bone, TV was calculated as the entire mineralized bone and marrow volumes, while BV encompassed the mineralized tissue volume of the cortical bone. In trabecular bone, TV was calculated as the entire bone marrow volume, while BV covered the mineralized part of this volume.

Table 1
List of abbreviations used in the dynamic microCT-based time-lapse bone morphometry with definition and unit.

Abbreviation	Definition	Unit
MV/BV	Normalized mineralized bone volume	–
EV/BV	Normalized eroded bone volume	–
MS/BS	Normalized mineralized bone surface	–
MS_{ST}/BS	Normalized mineralized bone surface-to-soft tissue interface	–
MS_{CB}/BS	Normalized mineralized bone surface-to-constant bone interface	–
ES/BS	Normalized eroded bone surface	–
ES_{ST}/BS	Normalized eroded bone surface-to-soft tissue interface	–
ES_{CB}/BS	Normalized eroded bone surface-to-constant bone interface	–
MAR	Mineral apposition rate	μm/days
MRR	Mineral resorption rate	μm/days

2.6. Analysis of spatial gradients in bone (re)modeling

Both the distal femoral metaphysis and the proximal tibial metaphysis were used for the spatial analysis of bone morphological changes. The femoral and tibial metaphysis (without the epiphysis) was discretized into intervals spanning 100 μm, starting at 400 μm from the end of the non-mineralized growth plate (on the interface with the primary spongiosa), reaching towards the diaphysis and ending at 1400 μm (resulting in 10 intervals), thereby covering nearly the entire ROI of 10% total bone length. The dynamic morphometry parameters were evaluated for each section separately at day 45 (with day 0 as a reference).

2.7. Reproducibility of image processing

To validate our image processing method, we determined the reproducibility of the registration and segmentation algorithm by calculating precision errors and confidence intervals of the matching of volumes and surfaces. To do so we used consecutive *ex vivo* scans microCT ($U\text{-}CT^{HR}$, MILabs, Netherlands) acquired on the same day. *Ex-vivo* microCT scans were used, since it has been shown that the reproducibility of *in vivo* and *ex vivo* scans is comparable [30]. The scans were performed on whole mice with intact limbs to approximate *in vivo* conditions. The tibiae of three mice (n = 6 bones) were scanned four times each on the same day, using the same settings as described for the *in vivo* image acquisition. Mice were repositioned after each scan and the results for the metaphysis are shown in Table S3, while results for the epiphysis are shown in Table S4 [18,31].

2.8. Code availability

The original code as well as the modified version used in this study are available on GitHub.

https://github.com/BWillieLab/Timelapse-Morphometry (original code)

https://github.com/CipitriaLab/Timelapse-Morphometry (modified code used in this study)

2.9. Sample preparation and Movat's Pentachrome staining

Bone specimens were cold embedded at 4 °C in poly(methyl methacrylate) (PMMA) (Technovit 9100, Kulzer, Germany), following the manufacturer's instructions. Briefly, samples were dehydrated in an ascending ethanol series, followed by a xylene washing, infiltration and embedding in PMMA. The staining was performed on 6 μm thick longitudinal sections using a standard protocol of Movat's Pentachrome [32]. The following tissue types were stained: mineralized bone and collagen (yellow), cartilage (blue/green), fibrin and muscle (red), cell nuclei (black). The stained sections were imaged with a Keyence Digital Microscope (VKX-5550E, Keyence, Germany).

2.10. Statistical analysis

The right femur and tibia of six animals were used for statistical evaluation. The plots show the mean and standard deviation. Normal distribution of the data was confirmed with the help of quartile-quartile plots. Paired *t*-tests were used for statistical comparison between different regions and parameters with significant differences presented as *$p \leq 0.05$, **$p \leq 0.01$ and ***$p \leq 0.001$. Origin 2021b (OriginLab, Northampton, US) was used to plot the data and for statistical analysis.

3. Results

3.1. Extended definitions of bone surface parameters and influence of bone surface curvature

Longitudinal imaging of cortical and trabecular bone (re)modeling revealed that different definitions of forming and resorbing bone surfaces can be used. Fig. 1B depicts a schematic with an example of the output of microCT scan registration, with mineralized (blue) and eroded (red) bone on constant bone (yellow). Fig. 1C and D illustrate four distinct surfaces, where we distinguish between a mineralizing (light blue) and eroding (light red) bone, and its interface to bone volumes that stayed constant (light yellow) or to surrounding soft tissue (black). This gives rise to four distinct surfaces:

- normalized mineralized bone surface-to-soft tissue interface (MS_{ST}/BS) (lined blue)
- normalized mineralized bone surface-to-constant bone interface (MS_{CB}/BS) (hatched blue)
- normalized eroded bone surface-to-soft tissue interface (ES_{ST}/BS) (lined red)
- normalized eroded bone surface-to-constant bone interface (ES_{CB}/BS) (hatched red)

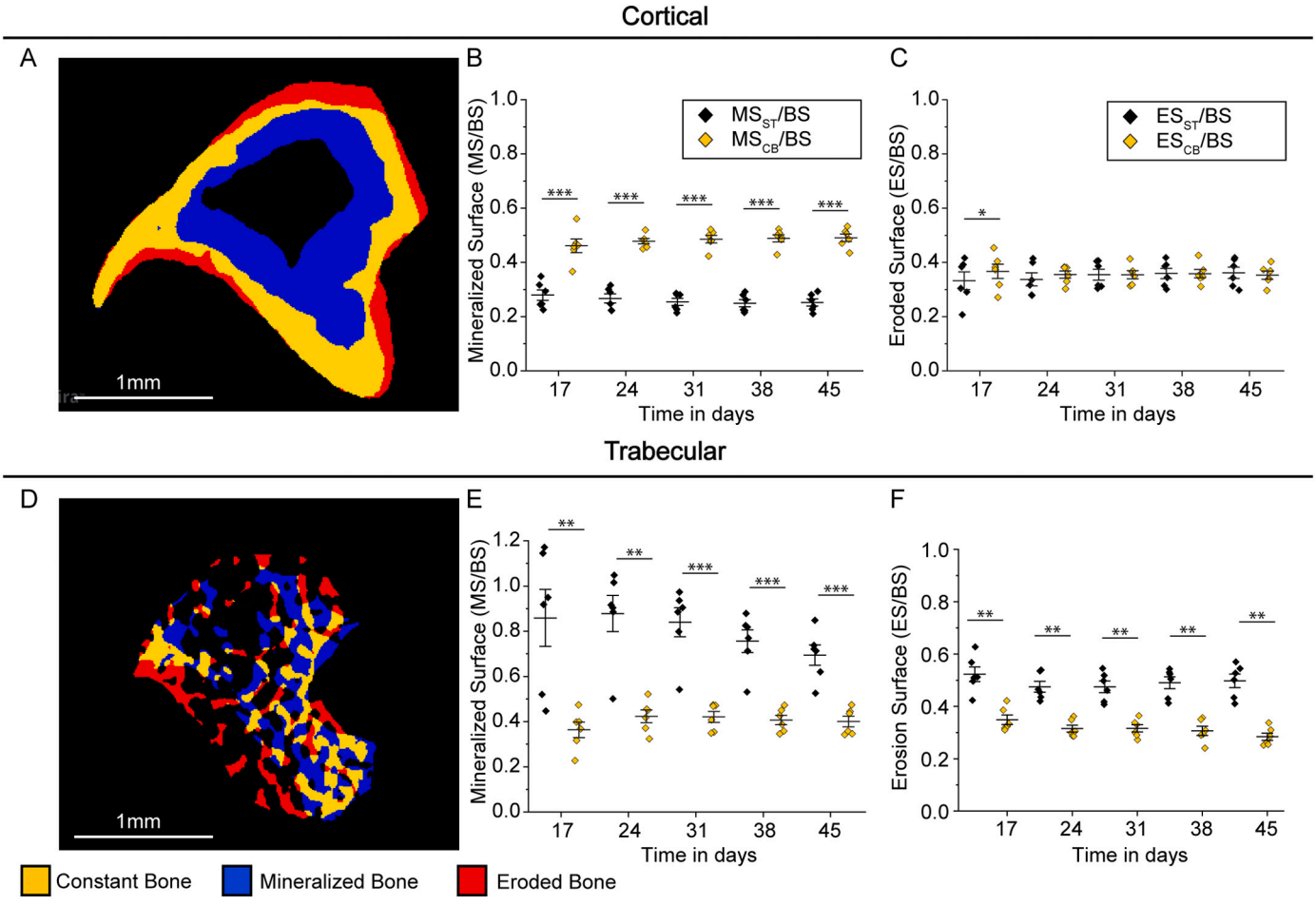

Fig. 2. Analysis of bone mineralization and erosion on four distinct interfaces that are strongly influenced by surface curvature. (A) Evaluation of bone (re)modeling of cortical bone (with constant bone in yellow, mineralized bone in blue and eroded bone in red, day 31). Shown are normalized (B) mineralized and (C) eroded surface over time, on the interface with constant bone (yellow) or with soft tissue (black). (D) Evaluation of bone (re)modeling of trabecular bone. Shown are normalized (E) mineralized and (F) eroded surface over time, on the interface with constant bone (yellow) or with soft tissue (black). All plots show mean and standard deviation, with statistically significant values presented as *$p \leq 0.05$, **$p \leq 0.01$ and ***$p \leq 0.001$. (For interpretation of the references to colour in this figure legend, the reader is referred to the web version of this article.)

Those surfaces are defined by the local curvature of the bone. On a flat surface, mineralization is often seen as a hill, leading to MS_{ST}/BS encompassing a larger surface as it covers the sides of the hill, while the MS_{CB}/BS intercepts the bottom of the hill and is therefore smaller. Similarly, the erosion is seen as a valley, as the ES_{ST}/BS runs along the top of the valley and is thus smaller than the ES_{CB}/BS which runs along the sides of the valley. The schemes in Fig. 1C show that on a convex surface, the (re)modeled bone and its interface with soft tissue (MS_{ST}/BS, ES_{ST}/BS) is larger than its interface with constant bone (MS_{CB}/BS, ES_{CB}/BS). The opposite holds true for a concave surface.

Cross sections of the tibia cortical (Fig. 2A) and trabecular (Fig. 2D) bone are depicted with constant bone in yellow, newly mineralized bone in blue and eroded bone in red. The evaluation of mineralized or eroded bone surface on the four distinct interfaces is shown for both cortical (Fig. 2B, C) and trabecular bone (Fig. 2E, F). The data is plotted over time with soft tissue interfaces (MS_{ST}/BS, ES_{ST}/BS) in black and constant bone interfaces (MS_{CB}/BS, ES_{CB}/BS) in yellow. The plots show the evolution of the interfaces over time and the significant differences of the respective surfaces to each other.

In the cortical bone compartment, mineralization mainly occurs within the endocortical region with a concave curvature (Fig. 2A). Consequently, the mineralized surface differs depending on the interface of choice, with the MS_{ST}/BS being significantly smaller than the MS_{CB}/BS (Fig. 2B). The values remain constant over time for both interfaces between day 17 and day 45. In contrast, erosion in the cortical bone mainly occurs on the periosteal side with both convex and concave regions (Fig. 2A). Therefore, it shows comparable results irrespective of the interface of choice (Fig. 2C), with values remaining constant over time.

In the trabecular bone compartment, only a small interface with

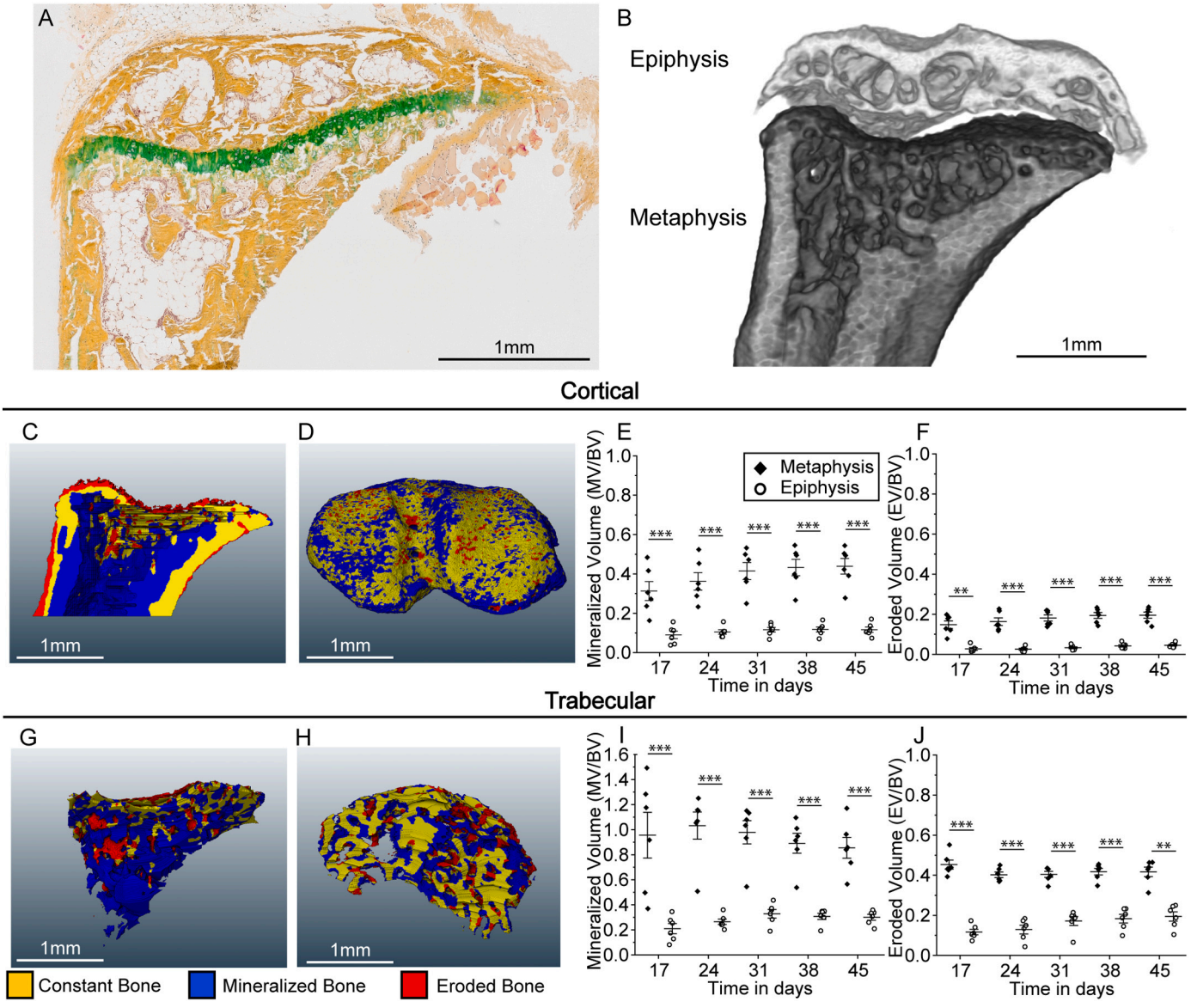

Fig. 3. Segmentation of ROI according to different (re)modeling behavior in metaphysis and epiphysis in the tibia. (A) Bone section stained with Movat's Pentachrome showing the growth plate (green/blue) and mineralized tissue (yellow). (B) Segmented microCT data with epiphysis (light grey) and metaphysis (dark grey). Evaluation of bone (re)modeling of cortical bone (with constant bone in yellow, mineralized bone in blue and eroded bone in red, day 31) in the (C) metaphysis and (D) epiphysis. Shown are normalized (E) mineralized and (F) eroded volume over time for metaphysis (diamond) and epiphysis (empty circle). Evaluation of bone (re)modeling of trabecular bone in the (G) metaphysis and (H) epiphysis. Shown are normalized (I) mineralized and (J) eroded volume over time, for metaphysis (diamond) and epiphysis (empty circle). All plots show mean and standard deviation, with statistically significant values presented as *$p \leq 0.05$, **$p \leq 0.01$ and ***$p \leq 0.001$. (For interpretation of the references to colour in this figure legend, the reader is referred to the web version of this article.)

constant bone exists as most of the trabecular bone is being (re)modeled (Fig. 2D). As a consequence, the mineralized (Fig. 2E) and eroded (Fig. 2F) surface on the interface with constant bone (MS_{CB}/BS, ES_{CB}/BS) are significantly smaller than on the interface with soft tissue (MS_{ST}/BS, ES_{ST}/BS), in both cases. This effect is stronger for the mineralized surface. MS_{ST}/BS shows a constant decrease over time from up to maximum 120% towards 90% (Fig. 2E), while all other three interfaces stay constant over time. In addition, no clear pattern of mineralization or erosion in specifically curved regions could be observed. The main influence on the results is the existence of constant bone, as the trabecular region is highly (re)modeled.

3.2. Metaphysis and epiphysis within the tibia exhibit different bone (re) modeling patterns

Longitudinal growth in mice continues past sexual maturity (6–8 weeks of age), albeit at a slower rate and the growth plate does not completely fuse and disappear. Thus, in mice the epiphysis and metaphysis do not fuse, but rather continue to be separated by the growth plate, with new cartilage formed at the epiphyseal side and cartilage replaced by new bone on the metaphyseal side. These specific regions of interest are visualized in the histological section on Fig. 3A, with mineralized tissue (yellow) separated by the growth plate (blue/green). To investigate, whether the metaphysis and epiphysis exhibit different bone (re)modeling patterns, we segmented these two ROIs using microCT data as shown in Fig. 3B, with the metaphysis in dark grey and the epiphysis in light grey. In addition, we measured the precision of our image registration method for both regions independently as presented in the supplementary in Table S3 for the metaphysis and Table S4 for the epiphysis.

Evaluation of bone (re)modeling in cortical bone using dynamic microCT-based time-lapse bone morphometry is depicted for the metaphysis in Fig. 3C as well as for the epiphysis in Fig. 3D. The quantitative analysis for normalized mineralized volume (MV/BV) over time is shown in Fig. 3E and normalized eroded volume (EV/BV) over time in Fig. 3F. The normalized mineralized volume of cortical bone ranges between 30 and 45% for the metaphysis, while it stays at approximately 10% for the epiphysis and is thus significantly different at all time points. This trend holds also true for the normalized erosion of cortical bone, where the eroded volume for the metaphysis is constant at around 20% and shows values of under 5% for the epiphysis, leading to significant differences at all time points.

Analogous results for trabecular bone including both primary and secondary spongiosa are depicted in Fig. 3G for the metaphysis and in Fig. 3H for the epiphysis. The quantitative analysis of the normalized mineralized volume (MV/BV) over time is shown in Fig. 3I and normalized eroded volume (EV/BV) over time in Fig. 3J. The normalized mineralized volume in the metaphysis trabecular bone spans a large range between 40 and 150% and shows an overall slight decrease over time. This is in accordance with the static microCT analysis (Fig. S3D–F), where BV increases from day 0 to day 17, and decreases again until day 45 (Fig. S3E). In the epiphysis the range is much smaller between 10 and 40% and is significantly lower than the mineralization in the metaphysis at all time points. The normalized eroded volume is similarly higher for the metaphysis (around 45%) than for the epiphysis (around 15%) with no visible changes over time but significant differences between metaphysis and epiphysis at each time point.

Overall, the segmentation and comparison of the cortical and trabecular bone in the metaphysis and the epiphysis shows that the two regions with distinct functions also exhibit different bone (re)modeling patterns, with significantly lower bone (re)modeling in the epiphysis compared to the metaphysis over the entire time range.

3.3. Mouse tibia and femur exhibit different bone (re)modeling patterns

The distal femur (Fig. 4A) and proximal tibia (Fig. 4B) regions in long bones of 12-week-old female BALB/c nude mice are located in close proximity to one another and share many morphological features. To compare the bone (re)modeling of the proximal tibia and the distal femur, volume, surface and mineral apposition/resorption rate (MAR/MRR) were studied in both cortical and trabecular bone as shown in Fig. 4. The newly introduced surface definitions (Figs. 1–2), as well as the distinct ROIs including the full growth plate (Fig. 3) were used for this analysis.

Cortical bone (re)modeling depicted in femur (Fig. 4C) and tibia (Fig. 4G), is quantified for mineralized/eroded volume (Fig. 4D, H), mineralized/eroded surface on four distinct interfaces (soft tissue interface in black and constant bone interface in yellow) (Fig. 4E, I) and mineral apposition/resorption rate (Fig. 4F, J) (with femur shown as diamond and tibia as empty circle in each plot).

In contrast to the femur, the tibia shows a strong mineralization front in the endocortical region (Fig. 4G). This is reflected in significantly higher mineralized volume (Fig. 4D) and mineral apposition rate (Fig. 4F) in the tibia *vs.* femur for every time point. A similar trend is observed for the mineralized surface on the interface with constant bone (MS_{CB}/BS) (Fig. 4E), where significant differences can be found at day 17, 31, 38 and 45. This indicates that the constant bone interface is the more sensitive interface to describe cortical bone mineralization.

Conversely, the femur and tibia do not differ in bone erosion (Fig. 4H–J) and both show stable erosion over time. The ES_{CB}/BS (Fig. 4I) though shows differences between femur and tibia, with a larger eroded surface for the femur over time, thus proving that the constant bone interface is the most sensitive to describe both mineralization and erosion events in the cortical bone compartment.

Trabecular bone (re)modeling depicted in the femur (Fig. 4K) and tibia (Fig. 4O), is quantified for mineralized/eroded volume (Fig. 4L, P), mineralized/eroded surface on four distinct interfaces (soft tissue interface in black and constant bone interface in yellow) (Fig. 4M, Q) and mineral apposition/resorption rate (Fig. 4N, R) (with femur shown as diamond and tibia as empty circle in each plot).

Analogous to cortical bone, mineralization in trabecular bone is significantly higher in the tibia *vs.* femur (Fig. 4L, M), although this only shows at later time points in the mineral apposition rate (Fig. 4N). The differences are significant for the mineralized volume (Fig. 4L) and on both mineralized surfaces (Fig. 4M).

In contrast to cortical bone, the erosion in trabecular bone as presented in Fig. 4P–R shows larger volumes and surfaces in the femur. The eroded surface on the interface with soft tissue (ES_{ST}/BS) (Fig. 4Q) shows significantly more erosion for the femur than for the tibia, thus making it the most sensitive interface to describe trabecular bone erosion. The mineral resorption rate (Fig. 4R) is also significantly higher for the femur than for the tibia, which would suggest localized erosion in the femur as can be seen in Fig. 4K.

3.4. Validation of dynamic bone (re)modeling with static microCT-based bone morphometry

To deepen the understanding and validate the results found for dynamic microCT-based bone morphometry, we evaluated the cortical and trabecular bone structure with the help of static microCT parameters. The data for tibial proximal metaphysis cortical bone is shown in Fig. S3A–C. TV is decreasing slightly over time (Fig. S3A), which is in accordance with the erosion found on the periosteal site visible in Fig. 3C. At the same time, BV is increasing over time, especially between day 0 and day 17, which is in accordance with MV/BV increasing over time and starting at around 0.3 (Fig. 4E). The data for tibial trabecular bone is shown in Fig. S3D - F. The decrease of TV is in accordance with the newly mineralized region on the endocortical bone reducing the overall marrow volume. BV on the other hand is first increasing between day 0 and day 17, but decreases after day 24 (Fig. S3E). The same trend is also seen in the MV/BV, which is high for day 17 and 24, but decreases afterwards (Fig. 4L).

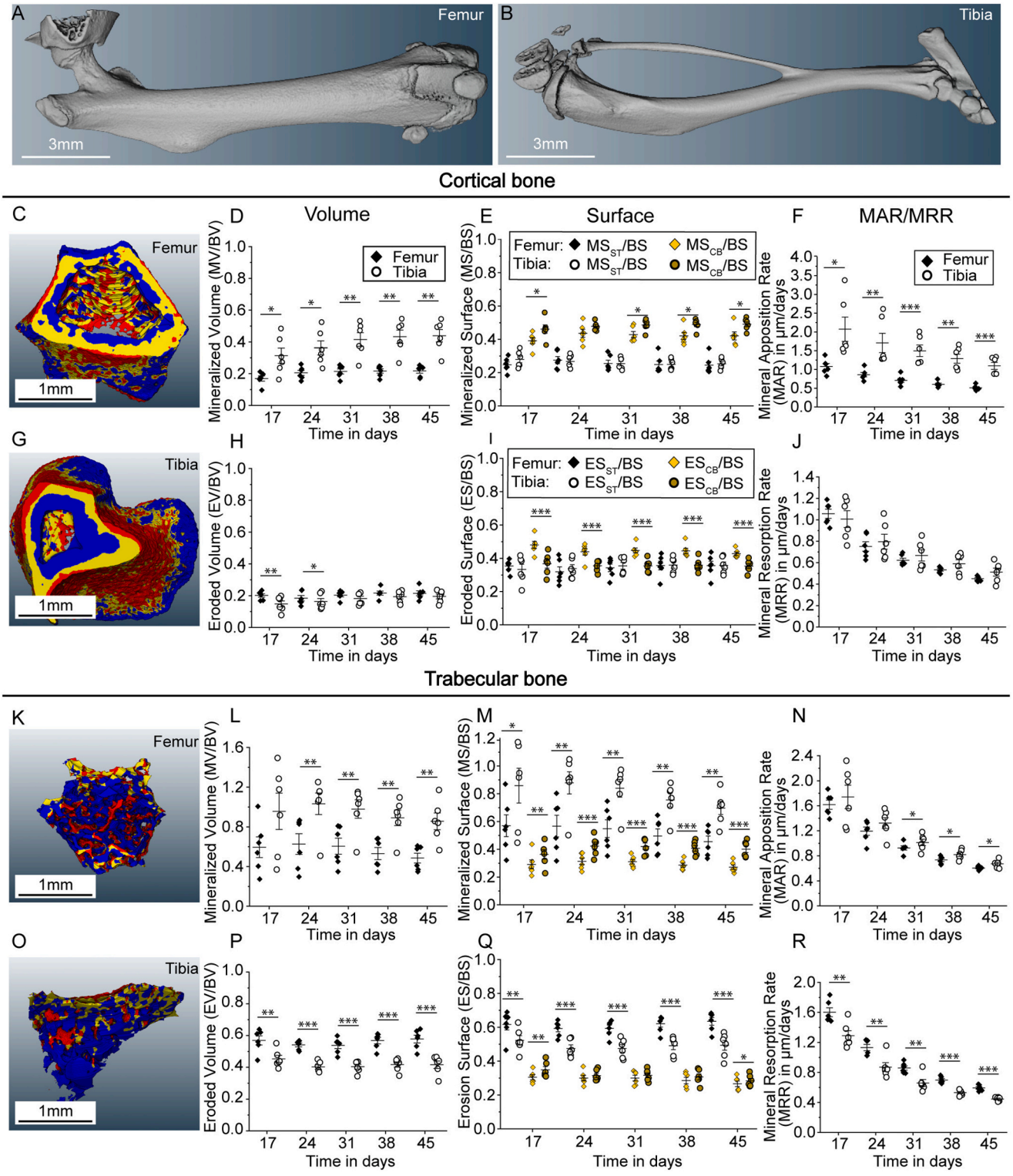

Fig. 4. Different bone (re)modeling patterns on the tibial proximal metaphysis and the femoral distal metaphysis. 3D rendering of microCT image of mouse (A) femur and (B) tibia. Evaluation of bone (re)modeling of cortical bone in the (C) femur and (G) tibia (day 31). Shown are normalized mineralized (D) volume, (E) surfaces (soft tissue interface in black and constant bone interface in yellow) and (F) MAR over time, as well as normalized eroded (H) volume, (I) surfaces (soft tissue interface in black and constant bone interface in yellow) and (J) MRR over time for femur (diamond) and tibia (empty circle). Evaluation of bone (re)modeling of trabecular bone in the (K) femur and (O) tibia (day 31). Shown are normalized mineralized (L) volume, (M) surfaces (soft tissue interface in black and constant bone interface in yellow) and (N) MAR over time, as well as normalized eroded (P) volume, (Q) surfaces (soft tissue interface in black and constant bone interface in yellow) and (R) MRR over time, for femur (diamond) and tibia (empty circle). All plots show mean and standard deviation, with statistically significant values presented as *$p \leq 0.05$, **$p \leq 0.01$ and ***$p \leq 0.001$. (For interpretation of the references to colour in this figure legend, the reader is referred to the web version of this article.)

The analysis of the tibial proximal metaphysis cortical bone surface as BS/BV shown in Fig. S4 reveals a large decrease between day 0 and day 17. This decrease can be expected with the endocortical mineralization visible in Fig. 2A. It also confirms the results we find in Fig. 2B, showing lower values for MS_{ST}/BS than for MS_{CB}/BS. Importantly, we find that only the dynamic analysis gives us detailed results on the different mineralized and eroded regions.

In Fig. S5 femoral distal metaphysis bone (re)modeling parameters are shown in direct comparison with tibial proximal metaphysis (Fig. S3). The analysis of the cortical bone TV (Fig. S5A) shows constant values for the femur in comparison with the slight decrease for the tibia. Cortical BV (Fig. S5B) stays also nearly constant for the femur, while it goes up for the tibia. This confirms the trend that was observed for MV/BV in Fig. 4D, showing nearly constant values for the femur but increasing values for the tibia. For trabecular bone, TV (Fig. S5D) is decreasing for both femur and tibia, with a much stronger trend in the tibia. BV (Fig. S5E) is slightly decreasing over time for the femur, while the tibia first increases and then decreases. These findings are in accordance with the dynamic analysis showing higher eroded volumes (Fig. 4P) and MRR (Fig. 4R) for the femur than the tibia.

To summarize, the static microCT analysis validates the findings of dynamic time-lapse microCT shown in Fig. 4 and depicts again the differences in tibial and femoral bone (re)modeling.

3.5. Spatial gradients in bone (re)modeling in the metaphysis of tibia and femur

Based on the observations that the metaphysis is highly dynamic compared to the epiphysis (Fig. 3) and that femur and tibia show significant differences in their (re)modeling behavior (Fig. 4), we then investigated if our model can detect and quantify spatial bone (re)modeling gradients in the metaphysis of cortical bone in the tibia and femur.

To do so we investigated the spatial (re)modeling of the cortical bone in the proximal tibia and distal femur at day 45 (in reference to day 0). The microCT scans were segmented into ten separate 100 μm thick sections starting 400 μm below the non-mineralized part of the growth plate (on the interface with the primary spongiosa) and reaching towards the diaphysis, as shown in Fig. 5A for the femur and in Fig. 5B for the tibia, with the orange lines indicating respective sections. With this, we covered nearly the full 10% bone length ROI of the metaphysis that was analyzed previously and is shown in Fig. 5A and B.

Normalized mineralized and eroded volume (Fig. 5C, E) and MAR and MRR (Fig. 5D, F) were analyzed (with the femur shown as diamond and the tibia as empty circle). Both femur and tibia show a gradient in mineralization visible for both the volume (Fig. 5C) and MAR (Fig. 5D), with increasing values from the growth plate towards the diaphysis and with a steeper gradient for the tibia than for the femur. These differences are significant already 500 μm below the growth plate and continue for the entire analyzed region.

In contrast, the eroded volume of both femur and tibia shows decreasing values from the growth plate towards the diaphysis (Fig. 5E), with a steeper drop for the femur. This leads to significantly higher eroded volumes in the femur for regions between 400 and 900 μm below the growth plate. In contrast to the mineralization rate MAR; the erosion rate MRR (Fig. 5F) shows constant values for most of the region analyzed, with only significantly higher values for the last sections (1200–1300 μm) of the tibia.

3.6. Pathological bone (re)modeling caused by breast cancer bone-metastatic early osteolytic events

The described methodology was tested to see if it could be a useful tool to detect larger disturbances in bone (re)modeling due to disease

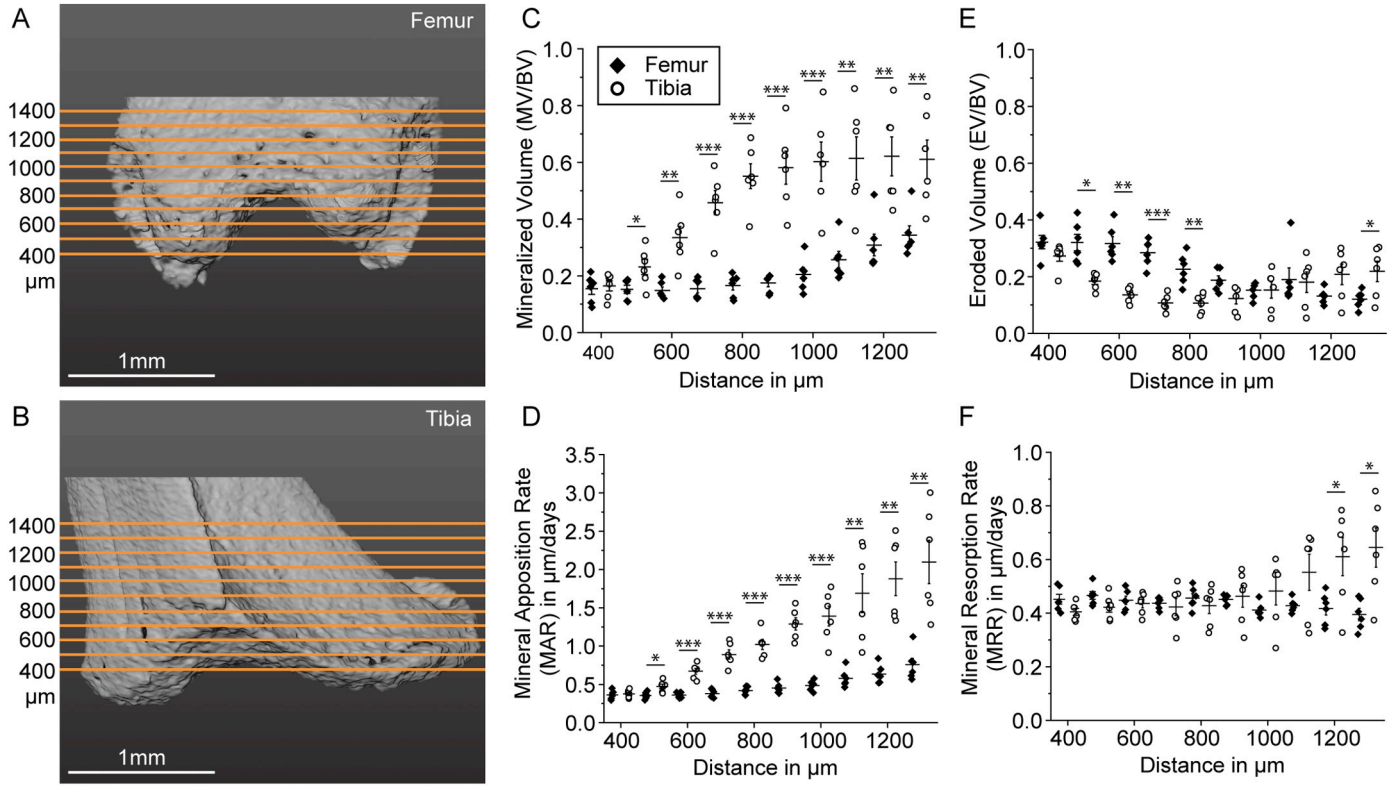

Fig. 5. Spatial evaluation of gradients in bone (re)modeling of femur and tibia reveals significant differences in mineralized regions. Localization of ten separate 100 μm thick sections in microCT images for (A) the femur and (B) the tibia. Shown are normalized cortical volume of (C) mineralization and (E) erosion as well as (D) MAR and (F) MRR, for femur (diamond) and tibia (empty circle) (for day 45). All plots show mean and standard deviation, with statistically significant values presented as *$p \leq 0.05$, **$p \leq 0.01$ and ***$p \leq 0.001$.

and quantify their spatio-temporal development, using the established differences between tibia and femur bone (re)modeling as a baseline. For this purpose, a pilot animal of a breast cancer bone metastasis model was employed, with an emerging osteolytic pathology in the distal femur (Fig. 6).

Cortical bone (re)modeling is depicted in evaluated microCT images at day 10 (Fig. 6A), day 17 (Fig. 6B), day 24 (Fig. 6C) and day 28 (Fig. 6D), showing constant bone in yellow, newly mineralized bone in blue and eroded bone in red. Already at day 17, a local accumulation of erosion pixels is observed in the posterior metaphysis between the condyles, which grows with time. The quantitative analysis of the cortical bone volume (Fig. 6E), surface (with soft tissue interface as diamond and constant bone interface as empty circle, Fig. 6F) and MAR/MRR (Fig. 6G) in the metaphysis are shown. An increase in normalized eroded volume compared to mineralized volume (Fig. 6E) and an increase in normalized eroded surface compared to mineralized surface (Fig. 6F) is detected already at day 17 and the difference increases at day 28. Surprisingly, this increase is not reflected in the change in mineralization or erosion rate shown by MAR and MRR (Fig. 6G). A comparison of mineralized (Fig. 6H) and eroded (Fig. 6I) volume of metaphysis and epiphysis was performed. Interestingly, the epiphysis (Fig. 6H, I) does not follow the same trend, thus is not affected by the osteolytic event. Lastly, spatial gradients of bone (re)modeling were investigated for the last time point (day 28), showing higher eroded volumes and a less steep decrease, while the mineralized volumes stayed constantly low (Fig. 6J).

Trabecular bone (re)modeling is depicted in evaluated microCT images at day 10 (Fig. 6K), day 17 (Fig. 6L), day 24 (Fig. 6M) and day 28 (Fig. 6N), clearly illustrating the expansion of the pathological site also in trabecular bone, as the eroded bone region (red) grows visibly over time, covering most of the trabecular bone already at day 24. The quantitative analysis of the bone volume (Fig. 6O), surface (with soft tissue interface indicated as diamond and constant bone interface as circle, Fig. 6P) and MAR/MRR (Fig. 6Q) are shown. Both bone volume and surface show decreasing values for the mineralization after day 17, in a seemingly linear way, and an increase in eroded volume and surface up to 90% at 28 days. In the surface evaluation, only the ES_{ST}/BS shows this trend, as most of the constant trabecular bone is resorbed, leaving little interface between eroded bone and constant bone and resulting in low values for both the mineralized and the eroded bone-to-constant bone interface. The MRR also shows initial high values followed by a gradual decrease after 17 days, while the MAR continues to decrease in a seemingly linear way (Fig. 6Q). A comparison of mineralized (Fig. 6R) and eroded (Fig. 6S) volume of metaphysis and epiphysis was performed. Analogous to cortical bone, the trabecular bone in the epiphysis (Fig. 6R, S) is not affected by the significant changes in the metaphysis and shows constant values. Finally, the effect of the pathology on both mineralization and erosion is clearly visible in Fig. 6T, where the ratio of both parameters (MV/EV) is shown, indicating a linear decrease after day 17, which provides a clear threshold criterion to define pathological (re)modeling.

4. Discussion

We build on microCT-based time-lapse morphometry methods by describing additional bone surface interface parameters and how they are influenced by bone curvature. We then use the method to investigate physiological cortical and trabecular bone (re)modeling in skeletally mature 12-week-old female BALB/c nude mice. In particular, we focus on the distal femur and proximal tibia, two regions in close proximity that share many morphological features. Nevertheless, we show significant and important differences in their (re)modeling behavior, by improving data preprocessing and expanding the previously established surface readout parameters. Specifically, we show variations between epiphysis and metaphysis, femur and tibia as well as spatial gradients within the metaphysis. This methodology is particularly powerful for setting a baseline of healthy bone (re)modeling not previously reported. This allowed us to then detect the onset of pathological bone (re)modeling and quantify its spatio-temporal evolution, as we show using early breast cancer bone metastasis as an example.

A critical point of analyzing microCT measurements is defining the right ROI [10]. As we have shown in Fig. 3, the (re)modeling behavior of the metaphysis and epiphysis of skeletally mature 12-week old mice are significantly different to each other, and those regions should therefore be analyzed separately and treated independently. This phenomenon can be explained by the differences in structural development, with the epiphysis originating from cartilaginous tissue that is ossified and thus less prone to (re)modeling [33]. Such difference could become smaller in elderly mice, where long bone growth has reached a plateau. The differentiation of the two regions is especially critical in cancer research, where the primary spongiosa close to the growth plate and the secondary spongiosa in the metaphyseal region are known to be one of the main targets for osteolytic lesions [34]. Even in the presence of clear osteolytic events in the metaphysis, the epiphysis is not affected (Fig. 6) and therefore should be excluded from the analysis of the bone (re)modeling parameters. This finding is in accordance with the work of He *et al.*, where the intact epiphysis is visible in histological sections even in case of large osteolytic lesions [35]. Conversely, not including the complete primary spongiosa in the analysis would lead to a lack of comprehensive information. Thus, the segmentation of the metaphysis and epiphysis offers the opportunity to study the effect of pathological (re)modeling in all necessary regions in the metaphysis without interference of non-affected regions in the epiphysis. This segmentation could also be interesting for other disease models like osteoarthritis, where the primary target is the subchondral bone and therefore the epiphysis [36].

We were able to show that four distinct surfaces can be described for the (re)modeling of bone, which are all strongly influenced by the local curvature of the bone and thus provide additional information on the spatio-temporal development of the bone structure. For the mineralization, the interface with the soft tissue (MS_{ST}/BS) is the surface visible after harvesting the bones and can therefore be described with static microCT or other imaging techniques. The MS_{CB}/BS on the other hand can only be studied in comparison to previous time points if the bone has been labeled, as is done in classical 2D histomorphometric analysis, which has been used to confirm microCT-based time-lapse morphometry [18]. A comparison of the two surfaces gives insight into the mineralization behavior, particularly for cortical bone, where bone geometry plays an important role. In the trabecular region, the changes of the distinct interfaces are strongly influenced by the overall (re)modeling of the bone. As trabecular bone is more drastically (re)modeled, the interface between constant and newly mineralized bone is significantly smaller compared to the soft tissue interface. The ES_{CB}/BS presents itself after the harvest of the bone, but can only be studied if prior knowledge of the bone status is available. The same holds true for the ES_{ST}/BS, which is already eroded and can thus only be studied with the help of time-lapse imaging. The ES is not frequently used in other studies but is of immense importance when studying osteolytic diseases [37]. The combination of both interfaces gives an important insight into the erosion geometry and the (re)modeling of the overall bone. To sum up, we could show that the constant bone interface is more sensitive to changes in the cortical bone, while the soft tissue interfaces is best suited to describe the (re)modeling in trabecular bone. The definition of four distinct surfaces and how they are being influenced by bone curvature is a completely new approach and can only be studied with microCT-based time-lapse morphometry. In the past only the interfaces relevant for a flat surface had been taken into account [18,19,22]. Here we were able to expand the spatial understanding of the (re)modeling process by describing all four relevant interfaces.

Especially in the surface evaluation, the threshold approach plays a critical role, as (re)modeling events can be missed or errors introduced. A common approach in the field is to use a fixed mean threshold [10]. It

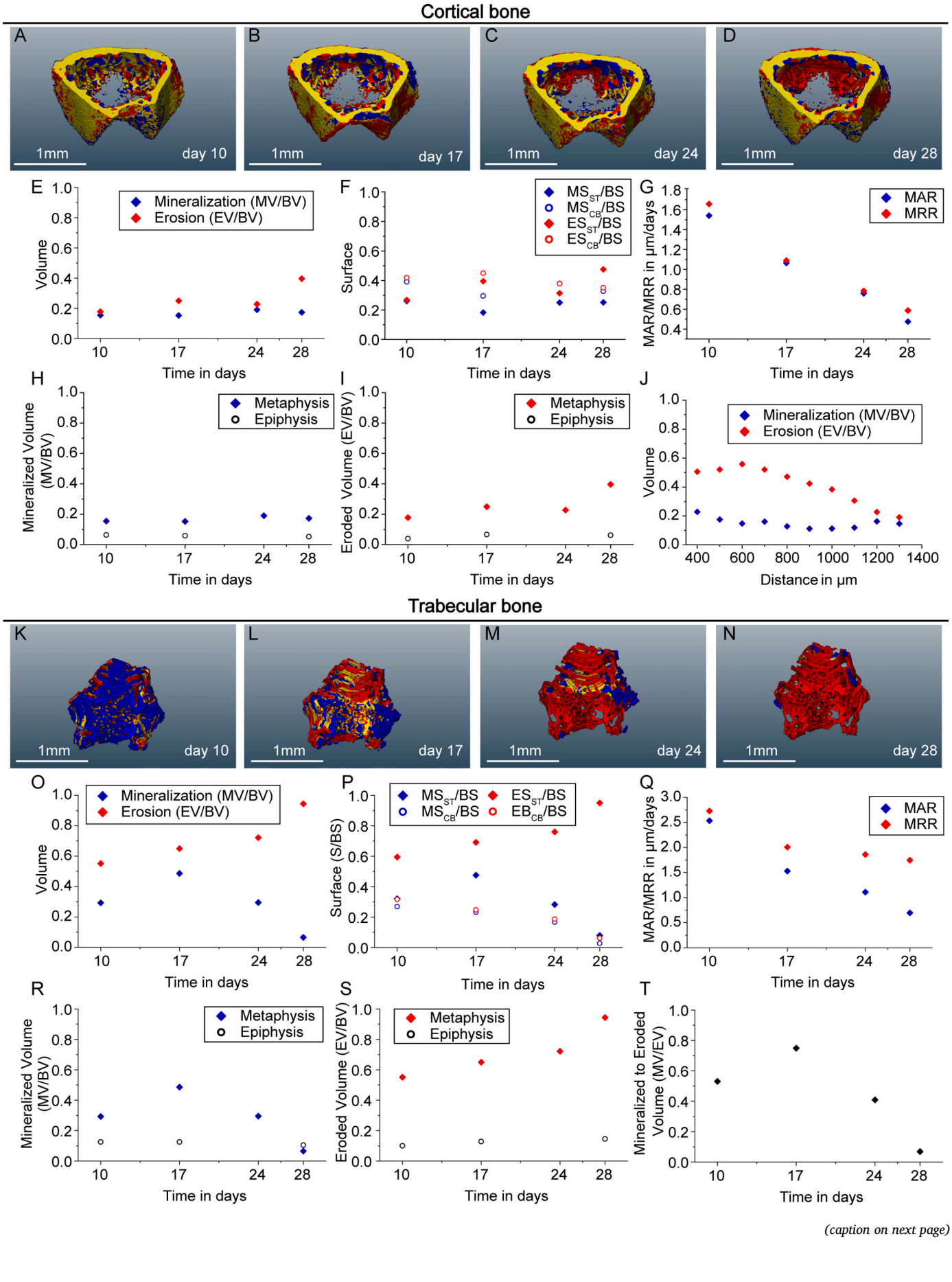

(caption on next page)

Fig. 6. Established baseline allows detection and tracking of an early breast cancer metastatic osteolytic event in the distal femoral metaphysis. Evaluation of bone (re)modeling of cortical bone at (A) day 10, (B) day 17, (C) day 24 and (D) day 28. Shown are normalized (E) volume, (F) surfaces (soft tissue interface as diamond and constant bone interface as empty circle) and (G) MAR/MRR over time with mineralization in blue and erosion in red. Comparison of metaphysis (diamond) and epiphysis (empty circle) for normalized (H) mineralized (blue) and (I) eroded (red) volume, as well as (J) spatial volume analysis of 100 μm sections with mineralization in blue and erosion in red. Evaluation of bone (re)modeling of trabecular bone at (K) day 10, (L) day 17, (M) day 24 and (N) day 28. Shown are normalized (O) volume, (P) surfaces (soft tissue interface as diamond and constant bone interface as empty circle) and (Q) MAR/MRR over time with mineralization in blue and erosion in red. Comparison of metaphysis (diamond) and epiphysis (empty circle) for normalized (R) mineralized (blue) and (S) eroded (red) volume, as well as (T) a ratio of mineralized and eroded volume. (For interpretation of the references to colour in this figure legend, the reader is referred to the web version of this article.)

is determined by calculating the threshold per ROI with a common method and then taking the mean of all, which is afterwards used as a fixed mean threshold for all ROIs. Other threshold approaches, such as variable thresholds, are applicable if the bone mineralization is not expected to be the same for all ROIs and time points. In our work, the differences in bone mineralization between the reference scan at day 0 and later time points, at day 17, 24, 31, 38 and 45, were significant as depicted in Fig. S2. In case of a fixed mean threshold, the mineralization of the reference scan (day 0) is underestimated as shown in Fig. S2G and H (only the orange voxels). The differences at day 45, on the other hand, are only very small, with very few additional voxels added on the surface (green voxels) when using a fixed mean threshold (Fig. S2O and P). Consequently, the mineralization is overestimated, mainly due to missing voxels in the reference scan at day 0 in case of a fixed mean threshold. Therefore, we believe that consistently using a variable threshold based on the Otsu method that best captures the increasing bone mineralization at each time point, and visually inspecting this for each scan, is the best approach in this dynamically changing setting, particularly since we compare small differences between the reference scan day 0 with day 17, 24, 31, 38 and 45.

In our study we compare the (re)modeling behavior in the proximal tibia and distal femur. Both regions have many physiological analogies and are used in investigations of bone (re)modeling or disease models. The established technique allowed us to find significant differences in the (re)modeling behavior of proximal tibia and distal femur, thus establishing a baseline of bone volume, surface and MAR/MRR for healthy bone (re)modeling. These results were validated with conventional static microCT analysis. The comparison shows that the femur is in a more stable state of homeostasis during the described age (12–18 weeks). The tibia shows higher new mineralization in both cortical and trabecular bone, which can be detected in volume, surface and MAR. The rationale behind the choice of selected parameters over many other possible dynamic histomorphometry parameters was to provide a broad picture of bone (re)modeling over time and use outcome measures that have previously been reported by others performing microCT-based time-lapse morphometry [18,19,22]. The combination of volume and surface gives both global and more detailed information about the areas of (re)modeling. The MAR and MRR describe the dynamics of these processes. Thus, with the selection of surface, volume and MAR/MRR parameters a precise and global result can be obtained in short time, which is especially important with time-lapse *in vivo* studies. Specifically the MAR obtained from *in vivo* microCT-based time-lapse morphometry had been compared by Birkhold *et al.* to standard 2D histomorphometry. They found slightly lower values for 3D microCT data, which could be explained by differences in resolution or a possible bias towards more dominant labels in the case of 2D histomorphometry [22]. The differences in bone (re)modeling we observed especially in cortical development may be related to the specific structure-function relationship due to biomechanical loading of tibia and femur in the mouse [38–40]. Furthermore, most bone loading studies are performed on the tibia [41], due to ease of experimental set-ups, but transfer of such limb loading data to the femur might be carefully re-considered in light of our findings. When comparing previously reported dynamic *in vivo* CT-based data to the results of this study, one can see that the diaphysis is (re) modeled far less [18], while the proximal tibia of 10 week-old BALB/c mice shows a similar trend of higher mineralization und lower erosion volume and surface [42]. The higher mineralization rate in the tibia is particularly interesting with regard to a study by Liu *et al.* who found that animals injected with tumor conditioned media had more bone growth, which could indicate a preference of cancer cell homing to newly mineralized sites and therefore the tibia overall [43]. With our study we have created a baseline for physiological bone (re)modeling using BALB/c nude mice, which is an important mouse strain used for studies in metastatic bone diseases that could prove useful for the investigation of early pathological or rare events.

In addition to the temporal evolution of tibia and femur, we also studied the spatial gradients in cortical bone (re)modeling in both regions, thus providing also a spatio-temporal reference for healthy bone. We showed that the tibia had more mineralization starting closer to the growth plate, that stayed significantly higher throughout the entire ROI. The femur on the other hand, showed higher eroded volumes closer to the growth plate, which needs to be considered when establishing osteolytic disease models.

The advanced technique investigating various bone surface interfaces, together with the baseline data for physiological bone (re) modeling, were used to detect pathological bone (re)modeling at an early stage and quantify the spatio-temporal development. We performed a pilot study with an early breast cancer bone metastasis mouse model on a different microCT scanner, which had been used in previous studies [18,22,23]. This resulted in a different but comparable voxel size. We used the described method to detect a pathological site at an early time point and track its spatio-temporal development, highlighting that the determined baseline parameters are not instrument specific. Rummler *et al.* [42] previously used time-lapse imaging to examine bone (re)modeling in a mouse model with established multiple myeloma bone disease. However, baseline parameters characterizing physiological (re) modeling of specific long bones were missing and are necessary to detect early bone (re)modeling changes at the onset of metastasis. Additionally, the proposed segmentation enables us to study early stages of metastasis in the primary spongiosa. The progression of the pathological site could be detected and quantified in trabecular bone, but only when the metaphysis and epiphysis were segmented and treated independently. Overall, we were able to characterize the sensitivity of our method, independently of the instrument, using this pilot animal with breast cancer bone metastasis.

The differences in the microCT scanners were clearly limiting the direct comparability of the baseline parameters with the tumor pilot animal. In addition, further experiments need to be conducted to achieve statistically relevant data for bone metastasis formation. Nevertheless, we were able to show that the new method presented may have potential to detect early pathological events and track spatio-temporal changes over time. In addition, this method may not be bound to a specific scanner, though validation on reproducibility and sensitivity of the method using different instruments is still required. Concerning the resolution, the analysis of early bone pathologies using time-lapse *in vivo* microCT is limited by a typical 8–10 μm voxel size. Lastly the influence of radiation has to be taken into account. Weekly or bi-weekly scans are necessary to follow and describe bone morphological changes in detail, in scenarios where rapid formation or resorption is occurring, leading to relatively high radiation exposure of the animals. Overall, the ability shown in this work to detect and track healthy and pathological bone (re)modeling will proof useful in the field.

5. Conclusions

Here we advance microCT-based time-lapse morphometry by expanding the surface evaluation with new definitions of bone surface interfaces and the effect of curvature, and improving the definitions of the ROIs according to their anatomical morphology and function. By doing so, we created a powerful tool to investigate 4D dynamics of bone (re)modeling that we used to define baseline parameters of changes in bone volume and surface over time, variations in the rate of the change, and spatial gradients thereof in the femoral and tibial metaphysis of skeletally mature 12-week-old female BALB/c nude mice. This quantification revealed anatomical site-specific differences in bone (re) modeling in tibia *vs.* femur. Furthermore, the method and quantitative baseline parameters were then tested to see if we could detect larger disturbances in bone homeostasis due to disease. In a pilot study with a breast cancer bone metastasis mouse model, the method shows the potential to detect the onset of a pathological osteolytic event and can track its spatio-temporal alterations over time. This method could have applications in various disease models with altered bone (re)modeling, including osteolytic alterations like breast cancer bone metastasis, multiple myeloma bone disease or osteoporosis, as well as osteoblastic alterations found in osteosarcoma or prostate cancer bone metastasis.

CRediT authorship contribution statement

Sarah A.E. Young: Methodology, Software, Validation, Formal analysis, Data curation, Writing – original draft, Writing – review & editing, Visualization, Project administration. **Maximilian Rummler:** Software, Data curation, Writing – review & editing. **Hubert M. Taïeb:** Software, Data curation, Writing – review & editing. **Daniela S. Garske:** Investigation, Writing – review & editing. **Agnes Ellinghaus:** Investigation, Writing – review & editing. **Georg N. Duda:** Resources, Writing – review & editing. **Bettina M. Willie:** Methodology, Resources, Data curation, Writing – review & editing. **Amaia Cipitria:** Conceptualization, Methodology, Resources, Data curation, Writing – review & editing, Supervision, Project administration, Funding acquisition.

Declaration of competing interest

The authors declare no conflict of interest.

Acknowledgement

This work was funded by the Deutsche Forschungsgemeinschaft (DFG) Emmy Noether grant (CI 203/2-1 to A. C., S.A.E. Y., D.S. G.). H.M. T. thanks the International Max Planck Research School (IMPRS) on Multiscale Bio Systems for financial support. M. R. and B. We thank the FRQS Programme de bourses de chercheur and Shriners Hospital for Children for funding. The work was partially supported by a grant to G. N. D. within the frame of the research group FOR 2165 funded by the Deutsche Forschungsgemeinschaft (DFG). We thank the lab of Dr. Joan Massagué at the Memorial Sloan Kettering Cancer Center, USA, for providing the MDA-MB-231-1883 BoM cells. The authors thank the technicians of the Research Workshop at the Charité-Universitätsmedizin Berlin for developing and manufacturing some experimental devices. We thank Mario Thiele, Jeannette Steffen and Isabela Vitienes for technical assistance with microCT measurements, histology and image analysis, respectively. The authors would like to acknowledge Peter Fratzl, Angelo Valleriani and Sadra Bakhshandeh for scientific discussion. BioRender has been used to draw the graphical illustration.

Appendix A. Supplementary data

Supplementary data to this article can be found online at https://doi.org/10.1016/j.bone.2022.116432.

References

[1] K.J. Jepsen, M.J. Silva, D. Vashishth, X.E. Guo, M.C. van der Meulen, Establishing biomechanical mechanisms in mouse models: practical guidelines for systematically evaluating phenotypic changes in the diaphyses of long bones, J. Bone Miner. Res. 30 (2015) 951–966, https://doi.org/10.1002/jbmr.2539.
[2] A.M. Parfitt, Osteonal and hemi-osteonal remodeling: the spatial and temporal framework for signal traffic in adult human bone, J. Cell. Biochem. 55 (1994) 273–286, https://doi.org/10.1002/jcb.240550303.
[3] H.M. Frost, Tetracycline-based histological analysis of bone remodeling, Calcif. Tissue Res. 3 (1969) 211–237, https://doi.org/10.1007/BF02058664.
[4] R. Hattner, B.N. Epker, H.M. Frost, Suggested sequential mode of control of changes in cell behaviour in adult bone remodelling, Nature 206 (1965) 489–490, https://doi.org/10.1038/206489a0.
[5] H.M. Frost, Skeletal structural adaptations to mechanical usage (SATMU): 3. The hyaline cartilage modeling problem, Anat. Rec. 226 (1990) 423–432, https://doi.org/10.1002/ar.1092260404.
[6] S. Kobayashi, H. Takahashi, A. Ito, N. Saito, M. Nawata, H. Horiuchi, H. Ohta, A. Ito, R. Iorio, N. Yamamoto, K. Takaoka, Trabecular minimodeling in human iliac bone☆, Bone 32 (2003) 163–169, https://doi.org/10.1016/S8756-3282(02)00947-X.
[7] A. Yajima, M. Inaba, Y. Tominaga, A. Ito, Bone formation by minimodeling is more active than remodeling after parathyroidectomy, Kidney Int. 74 (2008) 775–781, https://doi.org/10.1038/ki.2008.242.
[8] H. Saito, S. Takeda, N. Amizuka, Eldecalcitol and calcitriol stimulates 'bone minimodeling', focal bone formation without prior bone resorption, in rat trabecular bone, J. Steroid Biochem. Mol. Biol. 136 (2013) 178–182, https://doi.org/10.1016/j.jsbmb.2012.10.004.
[9] A.M. Parfitt, M.K. Drezner, F.H. Glorieux, J.A. Kanis, H. Malluche, P.J. Meunier, S. M. Ott, R.R. Recker, Bone histomorphometry: standardization of nomenclature, symbols, and units: report of the asbmr histomorphometry nomenclature committee, J. Bone Miner. Res. 2 (1987) 595–610, https://doi.org/10.1002/jbmr.5650020617.
[10] M.L. Bouxsein, S.K. Boyd, B.A. Christiansen, R.E. Guldberg, K.J. Jepsen, R. Müller, Guidelines for assessment of bone microstructure in rodents using micro-computed tomography, J. Bone Miner. Res. 25 (2010) 1468–1486, https://doi.org/10.1002/jbmr.141.
[11] R.L. De Souza, M. Matsuura, F. Eckstein, S.C.F. Rawlinson, L.E. Lanyon, A. A. Pitsillides, Non-invasive axial loading of mouse tibiae increases cortical bone formation and modifies trabecular organization: a new model to study cortical and cancellous compartments in a single loaded element, Bone 37 (2005) 810–818, https://doi.org/10.1016/j.bone.2005.07.022.
[12] J. Fritton, E. Myers, T. Wright, M. Vandermeulen, Loading induces site-specific increases in mineral content assessed by microcomputed tomography of the mouse tibia, Bone 36 (2005) 1030–1038, https://doi.org/10.1016/j.bone.2005.02.013.
[13] J.D. Boerckel, D.E. Mason, A.M. McDermott, E. Alsberg, Microcomputed tomography: approaches and applications in bioengineering, Stem Cell Res. Ther. 5 (2014) 144, https://doi.org/10.1186/scrt534.
[14] A. Cipitria, K. Boettcher, S. Schoenhals, D.S. Garske, K. Schmidt-Bleek, A. Ellinghaus, A. Dienelt, A. Peters, M. Mehta, C.M. Madl, N. Huebsch, D. J. Mooney, G.N. Duda, In-situ tissue regeneration through SDF-1α driven cell recruitment and stiffness-mediated bone regeneration in a critical-sized segmental femoral defect, Acta Biomater. 60 (2017) 50–63, https://doi.org/10.1016/j.actbio.2017.07.032.
[15] J.C. Reichert, A. Cipitria, D.R. Epari, S. Saifzadeh, P. Krishnakanth, A. Berner, M. A. Woodruff, H. Schell, M. Mehta, M.A. Schuetz, G.N. Duda, D.W. Hutmacher, A tissue engineering solution for segmental defect regeneration in load-bearing long bones, Sci. Transl. Med. 4 (2012), https://doi.org/10.1126/scitranslmed.3003720, 141ra93-141ra93.
[16] B.M. Willie, A.I. Birkhold, H. Razi, T. Thiele, M. Aido, B. Kruck, A. Schill, S. Checa, R.P. Main, G.N. Duda, Diminished response to in vivo mechanical loading in trabecular and not cortical bone in adulthood of female C57Bl/6 mice coincides with a reduction in deformation to load, Bone 55 (2013) 335–346, https://doi.org/10.1016/j.bone.2013.04.023.
[17] J.H. Waarsing, J.S. Day, J.C. van der Linden, A.G. Ederveen, C. Spanjers, N. De Clerck, A. Sasov, J.A.N. Verhaar, H. Weinans, Detecting and tracking local changes in the tibiae of individual rats: a novel method to analyse longitudinal in vivo micro-CT data, Bone 34 (2004) 163–169, https://doi.org/10.1016/j.bone.2003.08.012.
[18] A.I. Birkhold, H. Razi, G.N. Duda, R. Weinkamer, S. Checa, B.M. Willie, Mineralizing surface is the main target of mechanical stimulation independent of age: 3D dynamic in vivo morphometry, Bone 66 (2014) 15–25, https://doi.org/10.1016/j.bone.2014.05.013.
[19] F.A. Schulte, F.M. Lambers, G. Kuhn, R. Müller, In vivo micro-computed tomography allows direct three-dimensional quantification of both bone formation and bone resorption parameters using time-lapsed imaging, Bone 48 (2011) 433–442, https://doi.org/10.1016/j.bone.2010.10.007.
[20] A.R. Altman, W.-J. Tseng, C.M.J. de Bakker, A. Chandra, S. Lan, B.K. Huh, S. Luo, M.B. Leonard, L. Qin, X.S. Liu, Quantification of skeletal growth, modeling, and remodeling by in vivo micro computed tomography, Bone 81 (2015) 370–379, https://doi.org/10.1016/j.bone.2015.07.037.
[21] Y. Lu, M. Boudiffa, E. Dall'Ara, I. Bellantuono, M. Viceconti, Evaluation of in-vivo measurement errors associated with micro-computed tomography scans by means of the bone surface distance approach, Med. Eng. Phys. 37 (2015) 1091–1097, https://doi.org/10.1016/j.medengphy.2015.08.017.

[22] A.I. Birkhold, H. Razi, G.N. Duda, R. Weinkamer, S. Checa, B.M. Willie, The influence of age on adaptive bone formation and bone resorption, Biomaterials 35 (2014) 9290–9301, https://doi.org/10.1016/j.biomaterials.2014.07.051.
[23] A.I. Birkhold, H. Razi, G.N. Duda, R. Weinkamer, S. Checa, B.M. Willie, The periosteal bone surface is less mechano-responsive than the endocortical, Sci. Rep. 6 (2016) 23480, https://doi.org/10.1038/srep23480.
[24] A.I. Birkhold, H. Razi, G.N. Duda, S. Checa, B.M. Willie, Tomography-based quantification of regional differences in cortical bone surface remodeling and mechano-response, Calcif. Tissue Int. 100 (2017) 255–270, https://doi.org/10.1007/s00223-016-0217-4.
[25] A.I. Birkhold, A 4D Imaging Approach to Monitor Bone Remodeling, Technische Universität Berlin, Berlin, 2015 [dissertation].
[26] A.J. Minn, G.P. Gupta, P.M. Siegel, P.D. Bos, W. Shu, D.D. Giri, A. Viale, A. B. Olshen, W.L. Gerald, J. Massagué, Genes that mediate breast cancer metastasis to lung, Nature 436 (2005) 518–524, https://doi.org/10.1038/nature03799.
[27] Y. Kang, P.M. Siegel, W. Shu, M. Drobnjak, S.M. Kakonen, C. Cordón-Cardo, T. A. Guise, J. Massagué, A multigenic program mediating breast cancer metastasis to bone, Cancer Cell. 3 (2003) 537–549, https://doi.org/10.1016/S1535-6108(03)00132-6.
[28] V. Ponomarev, M. Doubrovin, I. Serganova, J. Vider, A. Shavrin, T. Beresten, A. Ivanova, L. Ageyeva, V. Tourkova, J. Balatoni, W. Bornmann, R. Blasberg, J. G. Tjuvajev, A novel triple-modality reporter gene for whole-body fluorescent, bioluminescent, and nuclear noninvasive imaging, Eur. J. Nucl. Med. Mol. Imaging 31 (2004) 740–751, https://doi.org/10.1007/s00259-003-1441-5.
[29] N. Otsu, A threshold selection method from gray-level histograms, IEEE Trans. Syst. Man. Cybern. 9 (1979) 62–66, https://doi.org/10.1109/TSMC.1979.4310076.
[30] H. Razi, A.I. Birkhold, P. Zaslansky, R. Weinkamer, G.N. Duda, B.M. Willie, S. Checa, Skeletal maturity leads to a reduction in the strain magnitudes induced within the bone: a murine tibia study, Acta Biomater. 13 (2015) 301–310, https://doi.org/10.1016/j.actbio.2014.11.021.
[31] C.C. Glüer, G. Blake, Y. Lu, B.A. Blunt, M. Jergas, H.K. Genant, Accurate assessment of precision errors: how to measure the reproducibility of bone densitometry techniques, Osteoporos. Int. 5 (1995) 262–270, https://doi.org/10.1007/BF01774016.
[32] H.Z. Movat, Demonstration of all connective tissue elements in a single section; pentachrome stains, AMA. Arch. Pathol. 60 (1955) 289–295, http://www.ncbi.nlm.nih.gov/pubmed/13248341 (accessed November 28, 2019).
[33] H.A. Cole, M. Yuasa, G. Hawley, J.M.M. Cates, J.S. Nyman, J.G. Schoenecker, Differential development of the distal and proximal femoral epiphysis and physis in mice, Bone 52 (2013) 337–346, https://doi.org/10.1016/j.bone.2012.10.011.
[34] G. Allocca, R. Hughes, N. Wang, H.K. Brown, P.D. Ottewell, N.J. Brown, I. Holen, The bone metastasis niche in breast cancer: potential overlap with the haematopoietic stem cell niche in vivo, J. Bone Oncol. 17 (2019), 100244, https://doi.org/10.1016/j.jbo.2019.100244.
[35] F. He, A.E. Chiou, H.C. Loh, M. Lynch, B.R. Seo, Y.H. Song, M.J. Lee, R. Hoerth, E. L. Bortel, B.M. Willie, G.N. Duda, L.A. Estroff, A. Masic, W. Wagermaier, P. Fratzl, C. Fischbach, Multiscale characterization of the mineral phase at skeletal sites of breast cancer metastasis, Proc. Natl. Acad. Sci. 114 (2017) 10542–10547, https://doi.org/10.1073/pnas.1708161114.
[36] N.C. Butterfield, K.F. Curry, J. Steinberg, H. Dewhurst, D. Komla-Ebri, N. S. Mannan, A.T. Adoum, V.D. Leitch, J.G. Logan, J.A. Waung, E. Ghirardello, L. Southam, S.E. Youlten, J.M. Wilkinson, E.A. McAninch, V.E. Vancollie, F. Kussy, J.K. White, C.J. Lelliott, D.J. Adams, R. Jacques, A.C. Bianco, A. Boyde, E. Zeggini, P.I. Croucher, G.R. Williams, J.H.D. Bassett, Accelerating functional gene discovery in osteoarthritis, Nat. Commun. 12 (2021) 1–18, https://doi.org/10.1038/s41467-020-20761-5.
[37] J. Vanderoost, From histology to micro-CT: measuring and modeling resorption cavities and their relation to bone competence, World J. Radiol. 6 (2014) 643, https://doi.org/10.4329/wjr.v6.i9.643.
[38] J. Prasad, B.P. Wiater, S.E. Nork, S.D. Bain, T.S. Gross, Characterizing gait induced normal strains in a murine tibia cortical bone defect model, J. Biomech. 43 (2010) 2765–2770, https://doi.org/10.1016/j.jbiomech.2010.06.030.
[39] A.C. Zumwalt, M. Hamrick, D. Schmitt, Force plate for measuring the ground reaction forces in small animal locomotion, J. Biomech. 39 (2006) 2877–2881, https://doi.org/10.1016/j.jbiomech.2005.10.006.
[40] D. Schmitt, A.C. Zumwalt, M.W. Hamrick, The relationship between bone mechanical properties and ground reaction forces in normal and hypermuscular mice, J. Exp. Zool.A Ecol. Genet. Physiol. 313A (2010) 339–351, https://doi.org/10.1002/jez.604.
[41] R.P. Main, S.J. Shefelbine, L.B. Meakin, M.J. Silva, M.C.H. Meulen, B.M. Willie, Murine axial compression tibial loading model to study bone mechanobiology: implementing the model and reporting results, J. Orthop. Res. 38 (2020) 233–252, https://doi.org/10.1002/jor.24466.
[42] M. Rummler, F. Ziouti, A.L. Bouchard, A. Brandl, G.N. Duda, B. Bogen, A. Beilhack, M.E. Lynch, F. Jundt, B.M. Willie, Mechanical loading prevents bone destruction and exerts anti-tumor effects in the MOPC315.BM.Luc model of myeloma bone disease, Acta Biomater. 119 (2021) 247–258, https://doi.org/10.1016/j.actbio.2020.10.041.
[43] A.E. Chiou, C. Liu, I. Moreno-Jiménez, T. Tang, W. Wagermaier, M.N. Dean, C. Fischbach, P. Fratzl, Breast cancer–secreted factors perturb murine bone growth in regions prone to metastasis, Sci. Adv. 7 (2021) 1–14, https://doi.org/10.1126/sciadv.abf2283.